UvA-DARE (Digital Academic Repository)

GRB 021004: Tomography of a gamma-ray burst progenitor and its host galaxy

Castro-Tirado, A.J.; Møller, P.; García-Segura, G.; Gorosabel, J.; Pérez, E.; de Ugarte Postigo, A.; Solano, E.; Barrado, D.; Klose, S.; Kann, D.A.; Castro Cerón, J.M.; Kouveliotou, C.; Fynbo, J.P.U.; Hjorth, J.; Pedersen, H.; Pian, E.; Rol, E.; Palazzi, E.; Masetti, N.; Tanvir, N.R.; Vreeswijk, P.M.; Andersen, M.I.; Fruchter, A.S.; Greiner, J.; Wijers, R.A.M.J.; van den Heuvel, E.P.J.

Link to publication

Astronomy & Astrophysics

GRB 021004: Tomography of a gamma-ray burst progenitor and its host galaxy⋆

A. J. Castro-Tirado[1], P. Møller[2], G. García-Segura[3], J. Gorosabel[1], E. Pérez[1], A. de Ugarte Postigo[4], E. Solano[5], D. Barrado[17,5], S. Klose[6], D. A. Kann[6], J. M. Castro Cerón[7], C. Kouveliotou[8], J. P. U. Fynbo[9], J. Hjorth[9], H. Pedersen[9], E. Pian[2,10,11], E. Rol[12,13], E. Palazzi[14], N. Masetti[14], N. R. Tanvir[12], P. M. Vreeswijk[9], M. I. Andersen[9], A. S. Fruchter[15], J. Greiner[16], R. A. M. J. Wijers[13], and E. P. J. van den Heuvel[13]

[1] Instituto de Astrofísica de Andalucía (IAA-CSIC), Glorieta de la Astronomía s/n, 18.008 Granada, Spain
e-mail: ajct@iaa.es
[2] European Southern Observatory, Karl-Schwarzschild-Strasse 2, 85748 Garching bei München, Germany
[3] Instituto de Astronomía, Universidad Nacional Autónoma de México, Apdo. Postal 877, Ensenada 22800, Baja California, México
[4] INAF, Osservatorio Astronomico di Brera, via E. Bianchi 46, 23807 Merate (LC), Italy
[5] Laboratorio de Astrofísica Estelar y Exoplanetas, Dpto. Astrofísica, Centro de Astrobiología (CSIC/INTA), PO Box 78, 28691 Villanueva de la Cañada, Madrid, Spain
[6] Thüringer Landessternwarte Tautenburg, Sternwarte 5, 07778 Tautenburg, Germany
[7] European Space Agency (ESA), European Space Astronomy Centre (ESAC), PO Box, Apdo. de correos 78, 28691 Villanueva de la Cañada, Madrid, Spain
[8] NASA Marshall Space Flight Center, NSSTC, 320 Sparkman Drive, Huntsville, Alabama 35805, USA
[9] Dark Cosmology Centre, Niels Bohr Institute, University of Copenhagen, Juliane Maries Vej 30, 2100 København Ø, Denmark
[10] INAF - Osservatorio Astronomico di Trieste, via Tiepolo, 11, 34131 Trieste, Italy
[11] Scuola Normale Superiore di Pisa, Piazza dei Cavalieri 7, 56126 Pisa, Italy
[12] Department of Physics & Astronomy, University of Leicester, University Road, Leicester LE1 7RH, UK
[13] Astronomical Institute "Anton Pannekoek", University of Amsterdam, PO number 94249, 1090 GE, Amsterdam, The Netherlands
[14] INAF - IASF di Bologna, via Gobetti 101, 40129 Bologna, Italy
[15] Space Telescope Science Institute, 3700 San Martín Dr, Baltimore, MD 21218-2463, USA
[16] Max-Planck-Institut für extraterrestrische Physik, 85748 Garching, Germany
[17] Calar Alto Observatory, Centro Astronómico Hispano Alemán, C. Jesús Durbán Remón, 2-2, 04004 Almería, Spain

ABSTRACT

Aims. We analyse the distribution of matter around the progenitor star of gamma-ray burst GRB 021004 and the properties of its host galaxy with high-resolution echelle and near-infrared spectroscopy.
Methods. Observations were taken by the 8.2 m Very Large Telescope with the Ultraviolet and Visual Echelle spectrograph (UVES) and the Infrared Spectrometer And Array Camera (ISAAC) between 10 and 14 h after the onset of the event.
Results. We report the first detection of emission lines from a GRB host galaxy in the near-infrared, detecting Hα and the [O III] doublet. These allow us to independently measure the systemic redshift ($z = 2.3304 \pm 0.0005$), which is not contaminated by absorption as the Lyα line is, and infer the host galaxy properties. From the visual echelle spectroscopy, we find several absorption-line groups spanning a range of about 3000 km s^{-1} in velocity relative to the redshift of the host galaxy. The absorption profiles are very complex with both velocity-broadened components extending over several 100 km s^{-1} and narrow lines with velocity widths of only ∼20 km s^{-1}. By analogy with QSO absorption line studies, the relative velocities, widths, and degrees of ionization of the lines ("line-locking", "ionization-velocity correlation") show that the progenitor had both an extremely strong radiation field and several distinct mass-loss phases (winds).
Conclusions. These results are consistent with GRB progenitors being massive stars, such as luminous blue variables (LBVs) or Wolf-Rayet stars, providing a detailed picture of the spatial and velocity structure of the GRB progenitor star at the time of explosion. The host galaxy is a prolific star-forming galaxy with a *SFR* of ∼40 $M_\odot$ yr^{-1}.

Key words. gamma-ray bust: general – techniques: spectroscopic – stars: Wolf-Rayet – galaxies: starburst – cosmology: observations

1. Introduction

The afterglows of long-duration gamma-ray bursts (GRBs), which are linked to the explosions of massive stars (see Woosley & Bloom 2006, for a review), are the most luminous optical sources in the universe for short periods of time (Kann et al. 2007; Bloom et al. 2009). Low-resolution optical spectroscopy

only was initially usable for determining the redshift and placed them at cosmological distances (Metzger et al. 1997). Deeper insight came with the first medium-resolution spectrum, obtained with Keck ESI, of the afterglow of GRB 000926 (Castro et al. 2003). The first true high-resolution echelle spectra were obtained for GRB 020813 (Fiore et al. 2005), but they were of low signal-to-noise ratio (hereafter *S/N*). The first echelle spectra of high *S/N* were finally obtained for GRB 021004, the focus of this work (see also Fiore et al. 2005).

⋆ Based on observations taken with the ESO's 8.2 m Very Large Telescope in Chile.

Spectroscopy allows deep insight into the environments of GRBs (Prochaska et al. 2006). Some highlights include the possible detection of a Galactic superwind in the host galaxy of GRB 030329 (Thöne et al. 2007), and variable absorption lines that result from direct UV pumping by the luminous GRB afterglow (Dessauges-Zavadsky et al. 2006; Vreeswijk et al. 2007; D'Elia et al. 2009). These detections have become possible for more afterglows due to the rapid localization capabilities of the *Swift* satellite (Gehrels et al. 2004) in combination with the rapid-response mode (RRM) now available for the Ultraviolet-Visual Echelle Spectrograph (UVES) at the Very Large Telescope (VLT) (e.g., Vreeswijk et al. 2007; D'Elia et al. 2009). The typical wavelength region has been increased to now extend from the ultraviolet into the K band near-infrared (nIR) by the second-generation instrument X-Shooter at VLT (D'Odorico et al. 2006; see de Ugarte Postigo et al. 2010, for a first result).

GRB 021004 was detected at 12:06:14 universal time (UT) on 2002, October 4 with the gamma-ray instrument FREGATE, the wide-field X-ray Monitor (WXM) and the soft X-ray camera (SXC) aboard the High-Energy Transient Explorer (*HETE-2*) (Shirasaki et al. 2002). GRB 021004, was a moderately bright, long-duration (T_{90} = 100 s) event with fluences of 6.4×10^{-7} erg cm^{-2} (7–30 keV) and 2.3×10^{-6} erg cm^{-2} (30–400 keV) (Barraud et al. 2002).

The GRB was rapidly localized in-flight and the position was reported in less than a minute, allowing rapid ground-based follow-up that identified the fading optical afterglow of GRB 021004 (Fox et al. 2003). This prompted follow-up observations at many observatories, including extensive long-term coverage at X-rays (Sako & Harrison 2002a,b), radio (Frail & Berger 2002; Berger et al. 2002; Pooley 2002a,b)[1], millimeter (de Ugarte Postigo et al. 2005), near-IR (de Ugarte Postigo et al. 2005; Fynbo et al. 2005), and optical wavelengths, both ground-based (Fox et al. 2003; Bersier et al. 2003; Uemura et al. 2003; Holland et al. 2003; Pandey et al. 2003; Mirabal et al. 2003; Kawabata et al. 2004; de Ugarte Postigo et al. 2005) and space-based (Fynbo et al. 2005).

The isotropic energy release during the prompt emission of this GRB was modest, with log E_{iso} = $52.65^{+0.12}_{-0.17}$ (Kann et al. 2010), and the dust extinction for this somehow reddish afterglow ($R - K \sim 3$) was also low as is typical of many well-observed afterglows (Kann et al. 2006). Despite the low amount of energy that was promptly released, this is among the most luminous afterglows ever detected (Kann et al. 2006), even compared to a much larger *Swift*-era sample (Kann et al. 2010). The multiwavelength temporal evolution of the GRB 021004 afterglow can be explained by multiple energy injections (Björnsson et al. 2004; de Ugarte Postigo et al. 2005), although other scenarios cannot be discarded (Lazzati et al. 2002). GRB 021004 remains one of the most well-observed afterglows ever.

Early-time low and medium resolution spectroscopic observations allowed a redshift of z = 2.33 to be determined on the basis of Ly-α absorption and emission lines (Chornock & Filippenko 2002). Several absorption systems with outflow velocities of a few 1000 km s^{-1} were also reported (Salamanca et al. 2002; Savaglio et al. 2002) and studied in detail by Møller et al. (2002b), Wang et al. (2003), Matheson et al. (2003), Schaefer et al. (2003), Mirabal et al. (2003), Starling et al. (2005), and Lazzati et al. (2006). Jakobsson et al. (2005) also

report the detection of the host galaxy Lyα line in narrow-band imaging.

Fiore et al. (2005) constrained the ionization parameters of the various absorption components detected above Lyα (at an observer rest-frame of 4050 Å) in GRB 021004, interpreting them as density fluctuations, as Lazzati et al. (2002) did. Within the context of larger samples, the UVES spectra of this GRB were also studied by Chen et al. (2007) (the general lack of wind signatures in high-resolution spectra of GRB afterglows), Prochaska et al. (2008) (N V absorption lines toward GRB afterglows), Fox et al. (2008) (high-ionisation line systems toward GRB afterglows), Tejos et al. (2007, 2009), and Vergani et al. (2009) (study of Mg II foreground absorption systems).

The original expectation, as detailed high quality spectroscopy of GRB afterglows became possible, was that we would rapidly learn much about the GRB progenitors by studying the complex absorption line systems they were expected to exhibit due to ejection events leading up to the final collapse. This expectation has thus far not been met.

Despite the large number of long GRB afterglow spectra that have now been obtained, GRB 021004 continues to be one with the most complex set of intrinsic (0–3000 km s^{-1} ejection velocity) absorption systems. At the time, it also held the place as the lowest detected HI column density, and it still ranks between the lowest seven measured. Its complexity originally suggested that it represented a display of ejecta (Møller et al. 2002a; Mirabal et al. 2003; Fiore et al. 2005) but this interpretation was later disputed by Chen et al. (2007). A final interpretation of the complex systems has not yet been agreed on, and this object remains the most probable candidate to exhibit rarely detected signatures of events prior to the collapse. The rarity alone would warrant a more detailed discussion of the spectral features. In addition, we include UVES data below 4050 ang for a more detailed discussion of the absorption systems (Sect. 3.1) and near-IR VLT/ISAAC spectroscopy allowing a more accurate determination of host properties and redshift (Sect. 3.2). We discuss our results in the light of progenitor models for GRBs in Sect. 4, and summarize our work in Sect. 5.

For a Hubble constant of H_0 = 72 km s^{-1} Mpc^{-1}, a matter density Ω_m = 0.3, and a cosmological constant Ω_Λ = 0.7, the luminosity distance to the host is d_L = 18.22 Gpc, and the look-back time is 10.42 Gyr. All errors are given at a 1σ level of confidence for a parameter of interest unless stated otherwise.

2. Observations and data reduction

2.1. Optical observations

Observations were conducted with 8.2-m Very Large Telescope Units 1 (VLT/UT1, Antu) and 2 (VLT/UT2, Kueyen) at the European Southern Observatory (ESO) in Cerro Paranal (Chile). We obtained optical spectroscopy of the GRB afterglow starting 0.6 days after the burst using the Ultraviolet-Visual Echelle Spectrograph (UVES) on UT2. Contemporaneous nIR observations were taken using the Infrared Spectrometer And Array Camera (ISAAC) on UT1 (see Table 1 for a log of the observations).

The optical data reduction was performed using the UVES context running under MIDAS[2]. The UVES context is structured into reduction recipes allowing for data reduction in a semi-automatic manner. A master bias frame was used for the bias

---

[1] See http://www.aoc.nrao.edu/~dfrail/grb021004.dat for the complete VLA data set.

[2] MIDAS (Munich Imaging Data Analysis System) is developed and maintained by the European Southern Observatory (ESO). http://www.eso.org/projects/esomidas/midas-distrib.html

Table 1. Journal of the VLT GRB 021004 optical/nIR spectroscopic observations.

UT Time (start)	Instr.	Exp. time (s)	Spectral range (Å)	S/N ratio[a]	Resolution $\lambda/\Delta(\lambda)$
03:02	UVES	3600	3290–4520	1	~56 000
			4620–5595	2.2	~51 500
			5675–6645	2.7	~51 500
03:02	ISAAC	3600	14 200–18 300	5.2	~500
04:10	UVES	3600	3050–3870	1	~51 300
			4780–5755	3.7	~50 500
			5835–6805	5.4	~50 500
05:15	UVES	3600	3750–4650	2.4	~51 500
			6705–8520	4.1	~52 300
			8665–10 400	2.2	~48 700
05:27	ISAAC	3000	18 400–25 800	2.3	~450

Notes. All observations were obtained on October 5 (UT).
[a] Per resolution element.

Table 2. Individual high-velocity metal-lines systems in GRB 021004.

Line ID	C2	C1	D	E2	E1
Si III $\lambda 1, 206$	y [a]	y	y	y	y
H I Lyα $\lambda 1, 216$	y	y	y	y	y
N V $\lambda 1, 238$–1, 242	y	–	–	–	y
Si II $\lambda 1, 260$–1, 264	–	y	?	–	y
C II $\lambda 1, 334$	y	y	–	–	–
Si IV $\lambda 1, 394$–1, 403	?	?	?	?	y
C IV $\lambda 1, 548$–1, 551	y	y	y	y	y
Al II $\lambda 1, 671$	–	y	–	y	y
Al III $\lambda 1, 855$–1, 863	–	–	–	–	y
Fe II $\lambda 2, 344$–2, 382	–	–	–	–	y
z	2.29671	2.29935	2.3216	2.3275	2.32891
v (km s^{-1})[b]	-3050[c]	-2810[d]	-795[e]	-262[f]	-134[g]

Notes. [a] y = yes; – = no; ? = doubtful, low significance due to low S/N in the S IV region. [b] Relative to the systemic velocity of the host galaxy at $z = 2.3304$, which we set as zero. [c] Embedded as C1 in the wide C complex (2730–3250 km s^{-1}). [d] Two subcomponents at -2837 and -2803 km s^{-1} (low ionization) and -2860 and -2810 km s^{-1} (high ionization). [e] Wide complex spanning 585–1005 km s^{-1}. [f] Embedded as E1 in the wide E complex (40–390 km s^{-1}). [g] Two subcomponents at -150 and -114 km s^{-1}.

subtraction. The order tracing was performed taking advantage of a first guess calibration solution based on the UVES physical model. In all cases, except for the red spectrum centered on 8600 Å, which is affected by fringing effects, the flat field correction was applied after the order extraction. A Th-Ar lamp was used for wavelength calibration. The spectra were extracted using an optimal extraction method, which provides the object signal and the variance. After the extraction, the spectra were resampled to constant wavelength bins and the orders merged into a single spectrum. Finally, both the standard heliocentric and vacuum wavelength corrections were applied.

2.2. Near-infrared observations

For the nIR observations, we used the short wavelength mode in low resolution, which yields a spectral coverage of 1.42–1.83 μm and 1.84–2.56 μm in the H and K bands, respectively. The pixel scale of the ESO-Hawaii detector is 0.′′146/pixel. For each band, 50 individual exposures of 60 s each were taken, shifting the target along the slit every 5 exposures in H (3 in K) to be able

to remove the sky background, a standard technique in infrared astronomy. We also collected dark and flat field images, which were used in the reduction process performed with IRAF[3]. After combining the groups of exposures and extracting the individual spectra, we calibrated them using the air-glow OH emission lines present in the 2 dimensional images. This allows an accurate wavelength calibration with dispersions of 4 and 8 Å/pix for H and K, respectively. Finally, the individual spectra were median-combined into a single one. In the case of the H band spectrum, we used a G2 spectral type star to remove the telluric absorption bands. The spectra were flux-calibrated by means of the JHK-band observations that we obtained either side of each science spectral observation.

3. Results

3.1. The blueshifted absorption-line systems

The VLT/UVES data set (Fig. 1) exhibits a large number of absorption lines, as well as Lyα in emission (see Table 3 for a list, and also Møller et al. 2002b; Starling et al. 2005; Jakobsson et al. 2005, on the Lyα emission line). Some of the absorption lines are due to two foreground systems at redshifts $z = 1.3820$ and $z = 1.6020$ (Møller et al. 2002b; Mirabal et al. 2003; see Tejos et al. 2007, 2009; and Vergani et al. 2009, for additional discussions about the foreground absorbers), but the remaining lines are from multiple systems found in the redshift range $2.2967 \leq z \leq 2.3291$.

In Fig. 2, we show the three wide absorption-line complexes in the redshift range $2.2967 \leq z \leq 2.3291$. The absorption profiles are plotted in velocity space and marked C, D, and E following the naming convention used by Møller et al. (2002a). The higher resolution of the UVES spectrum allowed us to identify four narrow line systems embedded inside the velocity structure of the broad systems C and E. We name those systems C1, C2, E1, and E2. In the following, we discuss all of those systems in more detail in order of increasing velocity relative to the host redshift ($z = 2.3304$, see Sect. 3.2).

E complex: The Lyα absorption width translates into velocities in the range 40–470 km s^{-1}, while in C IV (where we observe the narrowest trough), the range is 40–390 km s^{-1}. The difference in the high-velocity cut-offs (390 versus 470 km s^{-1}) is most easily understood as a column density effect, i.e., the column density of the high velocity end is too low for C IV to be detectable. Alternatively, it could be caused by lower metallicity in the higher velocity gas of system E, or a different ionization. The simplest interpretation of the E complex is that it is caused by gas, spanning velocities from 40–470 km s^{-1} and densities decreasing from the slowest to the fastest moving part. Similar profiles have been observed in QSO broad absorption line (BAL) systems, where velocities up to $\approx 0.1c$ have been found. BAL systems are interpreted as velocity broadening due to ejection and/or radiative acceleration. These BAL-like absorption troughs are not meaningfully fitted by standard (Voigt) profiles that assume a Gaussian velocity field.

Embedded in the E complex are two narrow-line systems at 134 km s^{-1} (E1) and 262 km s^{-1} (E2). The strongest component, E1, is divided equally into two subcomponents at 114 km s^{-1}

---

[3] IRAF is the Image Reduction and Analysis Facility, a general purpose software system for the reduction and analysis of astronomical data. IRAF is written and supported by the IRAF programming group at the National Optical Astronomy Observatories (NOAO) in Tucson, Arizona, USA.
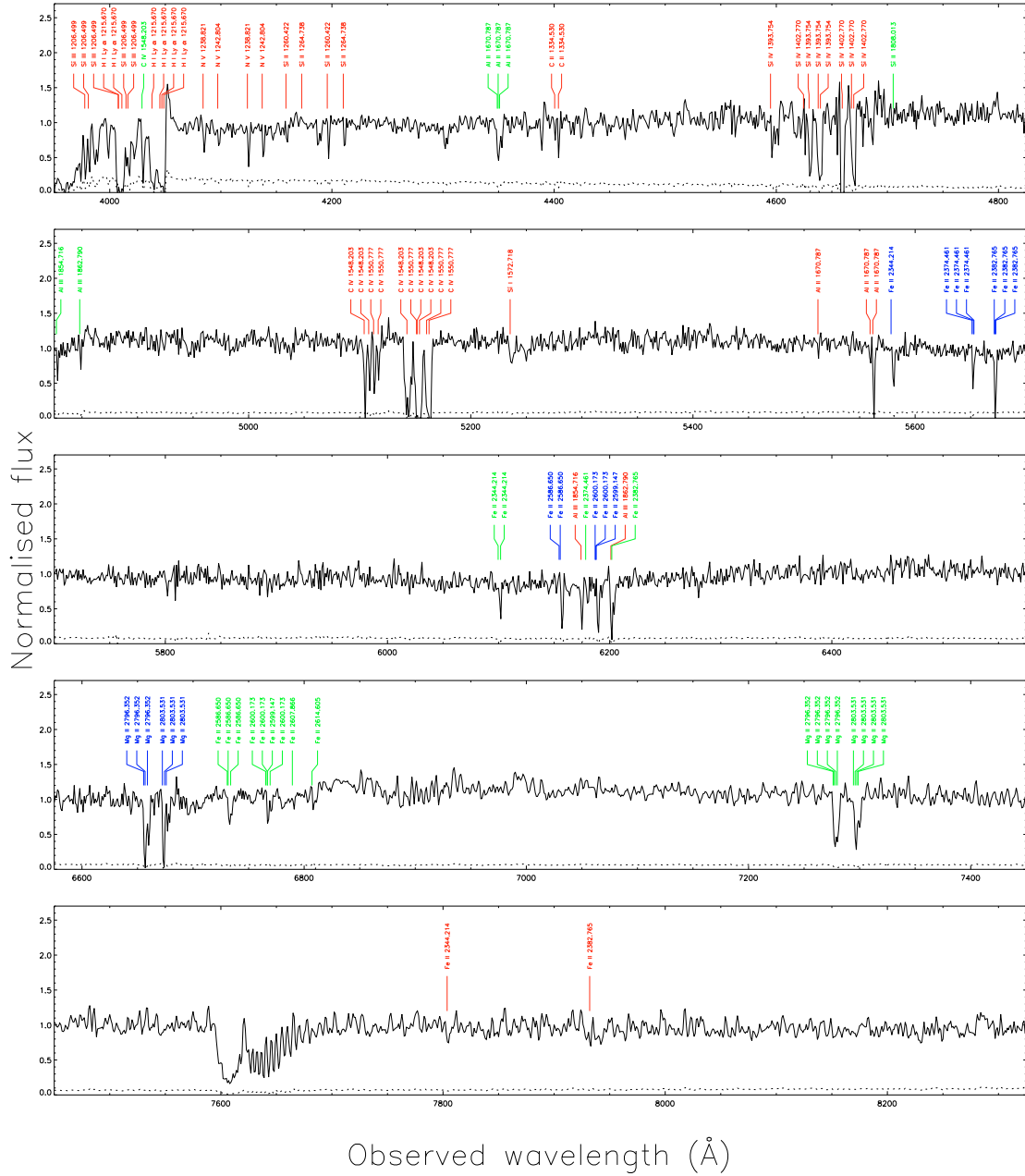
Fig. 1. Overall view of GRB 021004 optical afterglow spectrum. These VLT/UVES data were obtained ~0.6 days after the GRB and show the Lyα emission line arising from the host galaxy redshift plus some of the most prominent absorption lines systems at (or very close to) the host galaxy redshift: low ionization lines (such as Fe II, Si II) and high ionization lines (such as Si IV, C IV, N V), all labelled in red colour. Also shown for completeness are the absorption systems for the foreground systems at $z = 1.6020$ (labelled in green) and $z = 1.3820$ (labelled in blue). For clarity, the original data have been smoothed. The telluric lines in the *A*-band (7600–7630 Å) are noticeable. The dotted line is the error spectrum.

and 150 km s^{-1} (see Fig. 3) and exhibits absorption from a large number of both high and low ionic species (N V, C IV, Fe II, Al II, Al III, Si II, Si III, Si IV). The metal line absorption of E1 has similarities to so-called damped Lyα (DLA) systems, which in a few cases have been identified with high redshift, star-forming galaxies (Møller et al. 2002b) but it has too low HI column density along this sightline to be considered a DLA. Nevertheless, E1 is the system most likely to be identified with the interstellar medium (ISM) of the host galaxy of the GRB, whereby the velocity offset between the host and the ISM (~134 km s^{-1}) represents the velocity of the local absorbing cloud within the host. High and low ionic species are also seen in the second system (E2), but at lower significance. The

two rightmost dotted vertical lines in Fig. 2 mark the systems E1 and E2.

D Complex: The D complex consists of a single, wide BAL-like component seen in Lyα, C IV, and Si III. Both the C IV (1548 Å) and the Lyα troughs provide a consistent relative velocity range from 585 to 1005 km s^{-1}. We find residual flux at the bottom of both the Lyα and C IV (1548 Å) troughs indicating that the gas is optically thin. We also see significant variations in the optical thickness as a function of relative velocity; in particular, one may note the two sharp "dips" marking shells of higher column density at the leading and the trailing edges. Those dips are seen in Lyα, in both C IV lines and in Si III (marked by dotted lines in Fig. 2). The Si III trough is optically thick between those

Table 3. Line Identifications in the GRB 021004 OA spectra.

λ_{vacuum}(observed) (Å)	Line ID	EW (Å)^a	z
4008	H I Lyα 1215.670		2.2967
4015	Si III 1206.499		2.3275
4016	Si III 1206.499		2.3289
4028	C IV 1548.203		1.6024
4038	H I Lyα 1215.670		2.3216
4041	H I Lyα 1215.670		2.3243
4045	H I Lyα 1215.670		2.3275
4047	H I Lyα 1215.670		2.3289
4049^b	H I Lyα 1215.670		2.3304
4084.0	N V 1238.821	0.46 ± 0.16	2.2967
4097.2	N V 1242.804	0.35 ± 0.15	2.2967
4123.9	N V 1238.821	0.90 ± 0.14	2.3289
4137.2	N V 1242.804	0.66 ± 0.12	2.3289
4158.5	Si II 1260.422	0.25 ± 0.10	2.2993
4195.8	Si II 1260.422	0.71 ± 0.19	2.3289
4210.2	Si II 1264.738	0.51 ± 0.16	2.3289
4347.4	Al II 1670.787	0.49 ± 0.17	1.6020
4399.6	C II 1334.530	0.38 ± 0.15	2.2968
4403.0	C II 1334.530	0.79 ± 0.14	2.2994
4639.7	Si IV 1393.754	1.39 ± 0.83	2.3289
4669.7	Si IV 1402.770	1.29 ± 0.46	2.3289
5104.0	C IV 1548.203	1.77 ± 0.12	2.2967
5107.8	C IV 1548.203	0.16 ± 0.03	2.2992
5108.5	C IV 1548.203	0.84 ± 0.10	2.2998
5112.5	C IV 1550.777	1.15 ± 0.09	2.2967
5116.2	C IV 1550.777	0.06 ± 0.04	2.2992
5117.0	C IV 1550.777	0.67 ± 0.08	2.2998
5138.3	C IV 1548.203		2.3189
5140.0	C IV 1548.203		2.3200
5143.1	C IV 1548.203		2.3220
5146.7	C IV 1550.777		2.3188
5146.7	C IV 1548.203		2.3243
5148.5	C IV 1550.777		2.3200
5148.5	C IV 1548.203		2.3255
5151.7	C IV 1550.777		2.3220
5152.9	C IV 1548.203		2.3275+2.3289
5155.2	C IV 1550.777		2.3243
5157.6	C IV 1550.777		2.3255
5161.5	C IV 1550.777		2.3275+2.3289
5235.4	Si I 1572.718	0.80 ± 0.10	2.3289
5559.5	Al II 1670.787	0.23 ± 0.07	2.3275
5561.9	Al II 1670.787	1.73 ± 0.12	2.3289
5578.0	Fe II 2344.214	1.01 ± 0.15	1.3796
5651.2	Fe II 2374.461	0.52 ± 0.06	1.3800
5652.4	Fe II 2374.461	0.16 ± 0.05	1.3805
5652.9	Fe II 2374.461	0.13 ± 0.02	1.3807
5671.2	Fe II 2382.765	0.86 ± 0.07	1.3801
5671.9	Fe II 2382.765	0.41 ± 0.06	1.3804
5672.6	Fe II 2382.765	0.37 ± 0.06	1.3807
6099.6	Fe II 2344.214	0.59 ± 0.04	1.6020
6101.7	Fe II 2344.214	0.28 ± 0.04	1.6029
6154.5	Fe II 2586.650	0.67 ± 0.08	1.3794
6155.0	Fe II 2586.650	0.50 ± 0.09	1.3798
	Fe II 2365.552	0.50 ± 0.09	1.6020
6174.2	Al III 1854.716	1.15 ± 0.09	2.3289
6178.0	Fe II 2374.461	0.52 ± 0.08	1.6020
6187.0	Fe II 2600.173	0.67 ± 0.10	1.3794
6187.5	Fe II 2600.173	0.44 ± 0.08	1.3798
6188.0	Fe II 2599.147	0.50 ± 0.09	1.3808
6201.0	Al III 1862.790	0.73 ± 0.12	2.3289
6202.0	Fe II 2382.765	0.94 ± 0.16	1.6028
6654.0	Mg II 2796.352	1.95 ± 0.11*	1.3796
6655.5	Mg II 2796.352	1.95 ± 0.11*	1.3802
6657.0	Mg II 2796.352	0.71 ± 0.08	1.3808
6671.0	Mg II 2803.531	1.89 ± 0.41*	1.3796
6673.0	Mg II 2803.531	1.89 ± 0.41*	1.3802
6729.0	Fe II 2586.650	0.25 ± 0.07	1.6016
6730.2	Fe II 2586.650	0.60 ± 0.07	1.6020
6732.5	Fe II 2586.650	0.18 ± 0.06	1.6029
6764.0	Fe II 2600.173	0.56 ± 0.10	1.6015
6765.5	Fe II 2600.173	0.71 ± 0.09*	1.6020
	Fe II 2599.147	0.71 ± 0.09*	1.6030
6768.0	Fe II 2600.173	0.46 ± 0.09	1.6029
6788.0	Fe II 2607.866	0.14 ± 0.05	1.6030

Table 3. continued.

| λ_{vacuum}(observed) (Å)	Line ID	EW (Å)^a	z
7274.2	Mg II 2796.352	1.11 ± 0.10	1.6015
7275.5	Mg II 2796.352	0.83 ± 0.08	1.6020
7277.0	Mg II 2796.352	0.44 ± 0.07	1.6025
7278.5	Mg II 2796.352	0.83 ± 0.08	1.6029
7293.0	Mg II 2803.531	0.89 ± 0.09	1.6015
7294.5	Mg II 2803.531	0.98 ± 0.09	1.6020
7296.0	Mg II 2803.531	0.24 ± 0.06	1.6025
7297.0	Mg II 2803.531	1.00 ± 0.10	1.6029
7803.7	Fe II 2344.214	0.71 ± 0.28	2.3289
7931.8	Fe II 2382.765	0.46 ± 0.21	2.3288
16520^c	[O III] 4960.295	$-(16 \pm 7)$	2.3304
16679^d	[O III] 5008.240	$-(21 \pm 6)$	2.3304
21863^e	H I 6564.610	$-(37 \pm 10)$	2.3304

Notes. $^{(a)}$ Gaussian profile fitting (for non saturated lines only). Star symbols refer to complex systems. $^{(b)}$ Emission line. Partially absorbed, Lyα flux = $(1.5 \pm 0.2) \times 10^{-16}$ erg cm^{-2} s^{-1}. $^{(c)}$ Emission line [O III] flux = $(4 \pm 3) \times 10^{-17}$ erg cm^{-2} s^{-1}. $^{(d)}$ Emission line [O III] flux = $(12 \pm 3) \times 10^{-17}$ erg cm^{-2} s^{-1}. $^{(e)}$ Emission line Hα flux = $(11 \pm 2) \times 10^{-17}$ erg cm^{-2} s^{-1}.

two edges, but then appears to have an optically thin extension towards lower ejection velocities. However, this trough overlaps with Lyα of system C, and the extension is found to belong to system C (see below).

It is remarkable that the D and E systems are separated in velocity by exactly the amount required to shift the C IV 1550 Å line complex right on top of the C IV 1548 Å one in the spectrum (Møller et al. 2002b; Savaglio et al. 2002). This shift is known as absorption-absorption "line-locking" and is not uncommon in QSO spectra where radiative acceleration is important (e.g., Srianand et al. 2002). The line-locking between the D and E systems strongly suggests that a process similar to that seen in intrinsic QSO absorption systems is indeed involved here, i.e., radiative acceleration.

C Complex: As discussed above, the wide Lyα trough of system C is partly caused by Si III absorption from system D, but also contains Lyα absorption of a wide component spanning the velocity range 2730–3250 km s^{-1}, because we detect C II, C IV, Si II, Si III, Al II, and N V absorption in this velocity range (Fig. 2). The finely tuned velocity offset causing a precise overlap between the Lyα (C complex) and Si III (D complex) lines could be due to chance coincidence (although with small probability, see below). Given the evidence of line-locking between the two C IV lines between systems D and E, the overlap is most likely the result of radiative acceleration leading to line-locking of two expanding shells corresponding to the C and D complexes.

Embedded in C, we identify two narrow systems at 3050 km s^{-1} (C2) and at ~2810 km s^{-1} (C1). C2 is a high ionisation system that exhibits strong N V and C IV absorption, but no absorption from singly ionized ions. C1 is a low ionization system with moderate C IV absorption and clear detections of the singly ionized species Al II and Si II, which usually identifies a cloud optically thick at the Lyman limit (see Table 3). It is most likely that C2, although farthest away from the host redshift in velocity space, corresponds to the part of the wind that is nearest to the progenitor site in physical space. This ionization-velocity correlation is also observed in QSOs: the high ionization lines are often seen at the highest relative velocities for the $z_{abs} \approx z_{em}$ absorption systems in QSO spectra (e.g., Møller et al. 1994). As for E1, C1 consists of two subcomponents, detected at 2803 km s^{-1} and 2837 km s^{-1} (low ionization) and at
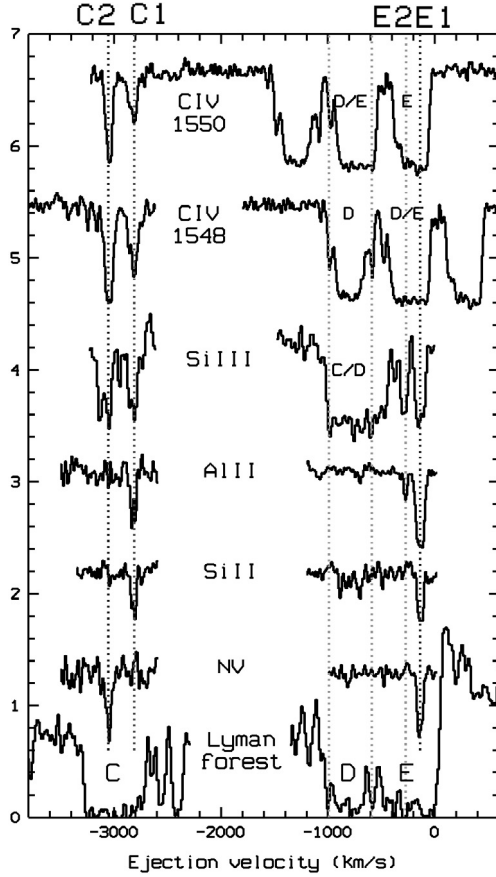
Fig. 2. In this figure, we have converted the observed wavelengths into velocities relative to the host redshift ($z = 2.3304$) for each ionic species significantly detected. Lyα is plotted at the bottom. To optimize the signal-to-noise ratio, two lines of N V (1238 and 1242 Å) and four lines of Si II (1260, 1264, 1533, and 1816 Å) have been coadded. The remaining lines are all single. The absorption components around $z \sim 2.3$ observed at velocities up to 3250 km s^{-1} are indicative of fast winds, ejected by a hot and massive stellar progenitor. The D and E complexes both contain velocity-broadened, BAL-like components. Within the E complex, there are narrow lines, E1 and E2, presumably from the ISM of the host galaxy. There are also narrow shells in the high-velocity system C, C1, and C2. The dotted lines indicate the positions of E1, E2, the "dips" at the leading and the trailing edges of D, and the C1 and C2 systems.

2810 km s^{-1} and 2860 km s^{-1} (high ionization). We again observe the ionization-velocity correlation seen already between C1 and C2 (Fig. 2). In a similar way to Fiore et al. (2005), we do consider C1 as part of the ejected systems simply on the basis of the low probability that is extrinsic, although we cannot exclude its association with the neighbouring galaxy detected by *HST* (Chen et al. 2007). In that case, it should be realized that the comparatively low H I column density reported by Fynbo et al. (2005) would be the sum of the H I column of the two galaxies, such that they both have even lower H I columns.

3.2. The near-IR emission lines

Assuming a redshift of the host of $z = 2.3351$ (Møller et al. 2002b, based on Lyα emission), we searched the ISAAC spectra for redshifted lines of H I (Hα, Hβ) and [O III] (4959 Å/5007 Å). There are tentative detections at low significance of Hα and the [O III] lines. To confirm the reality of the lines, we used the method that we introduced in Jensen et al. (2001). Our method
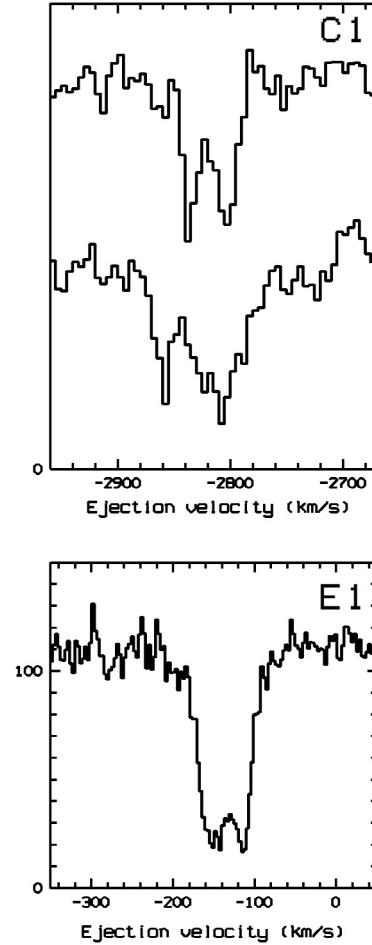
Fig. 3. A zoomed image of the high-resolution VLT/UVES spectrum at the location of the C1 and E1 narrow-line absorption systems. The data represent the coadded spectra of the different ions (N V + Si II + Al II + Al III) in velocity space. Thus, C1 has two subcomponents at 2803 km s^{-1} and 2837 km s^{-1} (low ionization, Si II + Al II, *top*) and 2810 km s^{-1} and 2860 km s^{-1} (high ionization, Si III + C IV, *bottom*). The ionization-velocity correlation also seen in QSOs (Møller et al. 1994) and WR nebulae (Smith et al. 1984) is noticeable. E1 divides equally into two subsystems at 114 km s^{-1} and 150 km s^{-1}.

briefly involves first rebinning the spectra into redshifts for the rest wavelength of each expected line, in our case the lines of Hα and [O III] (4959 Å/5007 Å). The three "redshift spectra" were then coadded (with weights 2, 1, and 1 because of the slightly higher *S/N* of the tentative Hα detection). The resulting combined line is clearly detected, as shown in Fig. 4.

To this combined line, we fitted a Gaussian (overplotted as a blue dotted line) and measured the systemic redshift to be $z = 2.3304 \pm 0.0005$, which is significantly different from the values derived from the Lyα emission line (which may be absorbed or modified by resonant scattering) or from the absorption systems (which are affected by the local velocity of the absorbing cloud in the host galaxy). The width of the Gaussian was found to be exactly the spectral resolution, so the lines are unresolved and we can place an upper limit on the intrinsic line width of 600 km s^{-1} *FWHM*.

Using a redshift of 2.3304 and the width of the resolution profile, we then fitted Gaussian profiles to the data (the continuum level and the amplitude of the Gaussian being the only free parameters) using min-square deviation. For the two [O III] lines, we also imposed a 1:3 flux ratio (Osterbrock 1989), we found
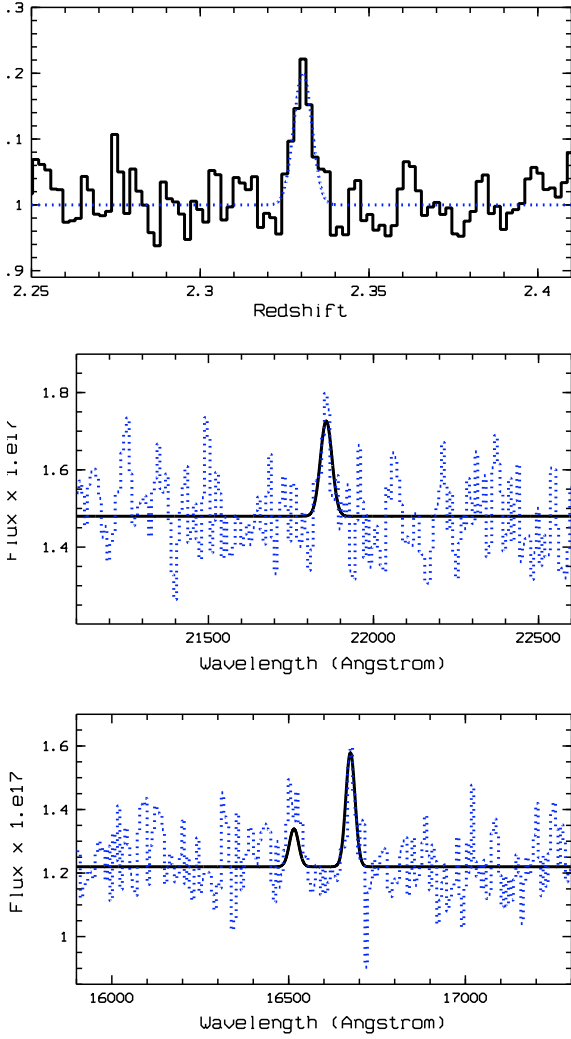
Fig. 4. *Bottom panels*: a zoomed image of the GRB 021004 nIR afterglow spectrum. These VLT/ISAAC data were obtained ~0.6 days after the GRB and show the Hα and [O III] emission lines arising from the host galaxy. *Top panel*: the coaddition of the three redshift spectra (as explained in the text) is shown, providing an independent measurement of the systemic redshift $z = 2.3304$ based on the nIR line emission. In the middle and bottom panels, we show the optimal fits (black), and the data itself (blue dotted).

the following fluxes: flux = $(4 \pm 1) \times 10^{-17}$ erg cm^{-2} s^{-1} ([O III] 4959 Å), $(12 \pm 3) \times 10^{-17}$ erg cm^{-2} s^{-1} ([O III] 5007 Å), and $(11 \pm 2) \times 10^{-17}$ erg cm^{-2} s^{-1} (Hα). The Hβ flux is consistent with zero.

4. Discussion

Following the suggestion that there is often a link between long-duration GRBs and core-collapse supernovae (Stanek et al. 2003; Hjorth et al. 2003) as proposed by Woosley (1993) we know that GRBs represent the end stages of massive-star evolution. As we now describe, the results presented here provide independent evidence of a massive star ($\geq 40\ M_{\odot}$) progenitor and additional insight into the immediate surroundings and prior evolution of the star leading up to the catastrophic event.

4.1. A LBV / Wolf-Rayet progenitor

The probability that the three absorption systems C1, C2, and D lie in front of the GRB host galaxy as a chance coincidence

is very small and can be computed using the number density of intervening C IV absorbers at $1.8 < z < 3.5$ of 1.5 ± 0.2 per unit redshift (Sargent et al. 1998). We find that the probability of finding three of them within the redshift range $\Delta z = 0.0337$ spanned by C1, C2, and D is $\sim 10^{-4}$. Fiore et al. (2005) used a similar argument but added the column densities to obtain an even lower probability. Like Fiore et al. (2005), we conclude that the absorbers must be intrinsic to the host galaxy. The large blueshift then makes it unlikely that the physical location can be anywhere else than close to the GRB progenitor.

Furthermore, the probability that the C IV 1550 Å line for complex E falls on top of the C IV 1548 Å line for complex D and that the Lyα line for system C falls on top of the Si III line for system D by chance is small, of order of a few percent for each, although difficult to quantify due to the complex profiles. Therefore, it makes sense to seek a physical explanation of the complex structure of the C, D, and E systems.

The multiple absorption-line systems found in the spectrum of GRB 021004 are naturally explained by multiple shell structures formed by the stellar winds of a massive progenitor star (Schaefer et al. 2003). These line-driven winds are expected for very massive stars (Castor et al. 1975; García Segura et al. 1996) that end their lives as Wolf-Rayet stars (WR) (de Koter et al. 1997), after passing through an unstable luminous blue variable (LBV) phase (Langer et al. 1999). Stellar evolution calculations for massive stars predict a number of different phases in which the wind properties associated with those phases, i.e., the velocities and mass-loss rates, become strongly time-varying (Langer et al. 1999; Maeder 1983). The minimum initial mass for a star to become a LBV is $\sim 40\ M_{\odot}$ (Langer et al. 1994; Maeder & Meynet 2000). During the course of their evolution, starting as O-class stars (O → LBV → WR → SN), stars have distinct winds in which their velocities are proportional to the escape velocities. Thus, for each transition where a fast wind (i.e., when the stellar radius was small) follows a slow one (larger stellar radius), a shell of swept-up material is formed. Within this simple scheme, computations of the circumstellar medium around a 60 $M_{\odot}$ star at the zero-age main sequence (García Segura et al. 1996) may produce the number of distinct compressed shells in the kinematic range seen in Fig. 2.

During the LBV phase, when hydrogen shell burning occurs, the stellar models are affected by several instabilities that cannot yet be modelled self-consistently and thus the unstable LBV phase cannot be fully resolved (Langer et al. 1994). However, several LBV observations show that a number of different swept-up shells can be formed. In particular, the D complex discussed above is akin to the Homunculus nebula around η Car, which contains $\sim 1\ M_{\odot}$ and expands at a speed in the range $700-1000$ km s^{-1} (Humphreys & Davidson 1994). As the formation of each of these swept-up shells occurs when the LBV reaches the Eddington limit (Langer et al. 1999), massive stars are able to form several compressed shells before ending their lives.

We note that, since the LBV stellar wind is asymmetric and often leads to a bipolar or at least asymmetric nebula (Gruendl et al. 2000), the GRB has to be beamed in the same direction as the wind for us to see the shells in absorption. Similar, but less spectacular, complex absorption has been detected in GRB 030226 (Klose et al. 2004; but see Shin et al. 2006) and GRB 050505 (Berger et al. 2006); this effect is not seen, however, in several other cases with similar quality data (Chen et al. 2007). It is possible, therefore, that GRBs for which no such complex velocity structure is seen have different relative orientations of
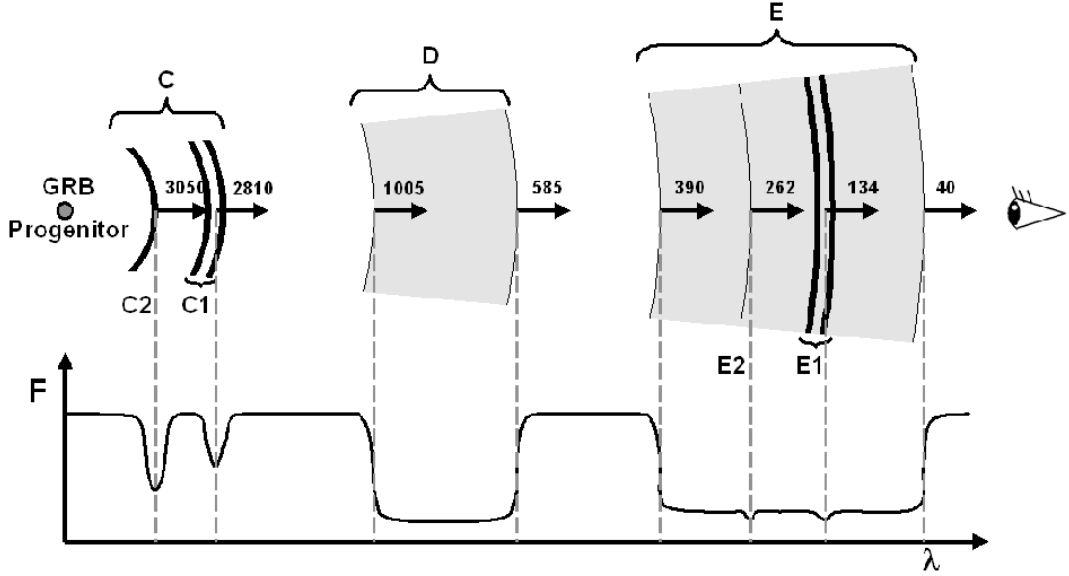
Fig. 5. A sketch showing the absorption-line complexes C, D, and E along the line of sight to GRB 021004, not drawn to scale. Velocities are given in km s^{-1}. Complex C, with the highest relative velocity, is most likely the closest to the progenitor site in space and is probably formed during the WR phase. The high-ionization sub-component C2 is the closest one to the progenitor whereas the colder sub-component C1 is further out and we cannot exclude that it could even be related to the neighbouring galaxy detected by *HST* (Chen et al. 2007). Complex E has the lowest relative velocity, and the broad part of the E complex is most likely caused by the oldest wind formed when the progenitor evolved from being an O star into the LBV phase or in the early LBV phase. The narrow E1 component has the properties expected for the ISM of the host galaxy. We believe that the D complex is caused by winds formed during the unstable LBV phase.

the wind and GRB jet. Highly ionized gas ($\sim T = 10^5$ K) of e.g., C IV, N V or Si IV, similar to that found in the environment of GRB 021004, has already been reported in a number of galactic ring nebulae surrounding Wolf-Rayet stars (Boronson et al. 1997). To form these gas shells, forward shocks moving at $\sim 10^2$ km s^{-1}, or reverse shocks at $\sim 10^2$–10^3 km s^{-1} are required. The most natural explanation of the C complex is that it was formed during the WR phase, with C1 and C2 lying in an expanding free wind, before reaching the shocked stellar wind. The ionization-velocity correlation seen in the systems C1 and C2 has also been detected in WR nebulae, but at lower velocities (~ 100–150 km s^{-1}; Smith et al. 1984).

In addition to the detailed picture of the spatial and velocity structure of the GRB progenitor star at the time of explosion (Fig. 5), our observations have also provided insight into the physical mechanism producing the progenitor shell structure. The C1 and C2 profiles are not P-Cygni, but almost symmetric profiles, thus ruling out their being very close to the burst (within ~ 0.2 pc) and accelerated by the GRB ionizing flux to the observed velocities, as has been proposed elsewhere (Schaefer et al. 2003; Mirabal et al. 2003). The detected line-locking also favours radiative acceleration by the progenitor star.

4.2. A starburst host galaxy

An extremely blue host galaxy was detected in late-time imaging (Fynbo et al. 2005; de Ugarte Postigo et al. 2005; Jakobsson et al. 2005). To derive the star-formation rate (SFR), we studied the emission lines seen in the combined optical-nIR spectrum.

The emission line parameters were measured by applying a Gaussian fit to the emission line and a flat fit to the continuum. If all the Hα emission is attributed to star formation in the host galaxy, we can compute the SFR to be SFR ($M_\odot$ yr^{-1}) $= 7.9 \times 10^{-42} L_{H\alpha}$ (erg/s) (Kennicutt et al. 1994). In our assumed cosmology, the measured Hα intensity transforms into a Hα

luminosity $L_{H\alpha} = (4.9 \pm 0.9) \times 10^{42}$ erg s^{-1}. This implies a SFR (without any corrections) of 40 ± 7 $M_\odot$ yr^{-1}, which is much higher than the present-day rate in our Galaxy. From the total measured Lyα intensity (Castro-Tirado et al. 2002), we derive a Lyα luminosity $L_{Ly\alpha} \leq (9 \pm 1) \times 10^{42}$ erg s^{-1}, which implies a $SFR \leq 10$ $M_\odot$ yr^{-1} in agreement with Fynbo et al. (2005) and Jakobsson et al. (2005). The Lyα/Hα ratio of 2 implies a low dust content in the GRB host galaxy, as also inferred by de Ugarte Postigo et al. (2005) and Kann et al. (2006) from the afterglow SED; there is also no excess absorption beyond the (low) Galactic value detected in *Chandra* X-ray observations (Sako & Harrison 2002a). This is a high value for the SFR (see also Castro-Tirado et al. 2007), although the S/N of the nIR spectrum implies a large uncertainty. The derived SFR implies that most of the ongoing star formation is unobscured, which is also in agreement with the SCUBA results at 850 μm (Tanvir et al. 2004).

The Lyα photons produced in the ionized nebula experience a continuous resonant scattering in the presence of HI. In a dust-free nebula, this mechanism effectively traps the Lyα photons producing a typical P Cygni line profile in both emission and absorption, depending on the details of the density and velocity field. However, if even a little dust is present, most Lyα photons will disappear by heating dust grains, because radiation absorption by dust has a maximum cross-section close to the wavelength of Lyα. Thus, the observed complex Lyα profile is the result of both mechanisms, resonance scattering which determines the profile shape, and dust absorption, which decreases yet further the intensity of the emission line. The Lyα P Cygni profile can be understood in terms of these mechanisms acting during the evolution of the swept-up HI supershell produced by a massive starburst in the host galaxy of GRB 021004. It corresponds to stage 4 in the evolutionary scheme developed by Tenorio-Tagle et al. (1999) and Más-Hesse et al. (2003), a stage compatible with GRB 021004 being the evolution endpoint of a WR star.

5. Conclusions

We have identified several absorption line groups spanning a range of about 3000 km s^{-1} in velocity relative to the redshift of the host galaxy. The absorption profiles are very complex with both velocity-broadened components extending over several 100 km s^{-1} and narrow lines with velocity widths of only ~20 km s^{-1}. By analogy with QSO absorption line studies, the relative velocities, widths, and degrees of ionization of the lines ("line-locking", "ionization-velocity correlation") show that the progenitor had both an extremely strong radiation field and several distinct mass-loss phases (winds). These results are consistent with GRB progenitors being massive stars, such as LBVs or Wolf-Rayet stars, and provides additional insight into the nature of these progenitors and their immediate environments.

The host galaxy is a prolifically star-forming galaxy at a systemic redshift $z = 2.3304$, which has a *SFR* of ~40 $M_\odot$ yr^{-1} as also found by Fynbo et al. (2005) and de Ugarte Postigo et al. (2005), reinforcing the potential association of some GRB with starburst galaxies (Christensen et al. 2004; Gorosabel et al. 2005, and references there in).

The *Swift* mission with a predicted lifetime of ten years (Gehrels et al. 2004) will certainly provide us the opportunity to carry out high-resolution spectroscopy for dozens of future GRBs, and to ascertain physical/chemical properties common to all GRB outflows.

References

Barraud, C., Olive, J.-F., Lestrade, J. P., et al. 2002, A&A, 400, 1021
Berger, E., Frail, D. A., & Kulkarni, S. R. 2002, GCN Circ., 1613, http://gcn.gsfc.nasa.gov/gcn3/1613.gcn3
Berger, E., Penprase, B. E., Cenko, S. B., et al. 2006, ApJ, 642, 979
Bersier, D., Stanek, K. Z., Winn, J. N., et al. 2003, ApJ, 584, L43
Björnsson, G., Gudmundsson, E. H., & Jóhánesson, G. 2004, ApJ, 615, L77
Bloom, J. S., Perley, D. A., Li, W., et al. 2009, ApJ, 691, 723
Boroson, B., McCray, R., Oelfke Clark, C., et al. 1997, ApJ, 478, 638
Castor, J. I., Abbott, D. C., & Klein, R. I. 1975, ApJ, 195, 157
Castro, S., Galama, T. J., Harrison, F. A., et al. 2003, ApJ, 586, 128
Castro-Tirado, A. J., Pérez, E., Gorosabel, J., et al. 2002, GCN Circ., 1635, http://gcn.gsfc.nasa.gov/gcn3/1635.gcn3
Castro-Tirado, A. J., Bremer, M., McBreen, S., et al. 2007, A&A, 475, 101
Chen, H.-W., Prochaska, J. X., Ramirez-Ruiz, E., et al. 2007, ApJ, 663, 420
Chornock, R., & Filippenko, A. 2002, GCN Circ., 1605, http://gcn.gsfc.nasa.gov/gcn3/1605.gcn3
Christensen, L., Hjorth, J., & Gorosabel, J. 2004, A&A, 425, 913
de Koter, A., Heap, S. R., & Hubeny, I. 1997, A&A, 477, 792
de Ugarte Postigo, A., Castro-Tirado, A. J., Gorosabel, J., et al. 2005, A&A, 443, 841
de Ugarte Postigo, A., D'Elia, V., Goldoni, P., et al. 2010, A&A, 513, A42
D'Elia, V., Fiore, F., Perna, R., et al. 2009, ApJ, 694, 332
Dessauges-Zavadsky, M., Chen, H.-W., Prochaska, J. X., Bloom, J. S., & Barth, A. J. 2006, ApJ, 648, L89
D'Odorico, S., Dekker, H., Mazzoleni, R., et al. 2006, in SPIE Conf. Ser., 6269
Fiore, F., D'Elia, V., Lazzati, D., et al. 2005, ApJ, 624, 583
Fox, D. W., Yost, S., Kulkarni, S. R., et al. 2003, Nature, 422, 284
Fox, A. J., Ledoux, C., Vreeswijk, P. M., Smette, A., & Jaunsen, A. O. 2008, A&A, 491, 189
Frail, D. A., & Berger, E. 2002, GCN Circ., 1574, http://gcn.gsfc.nasa.gov/gcn3/1574.gcn3
Fynbo, J. P. U., Gorosabel, J., Smette, A., et al. 2005, ApJ, 633, 317
García-Segura, G., Mac Low, M.-M., & Langer, N. 1996, A&A, 305, 229
Gehrels, N., Chincarini, G., Giommi, P., et al. 2004, ApJ, 611, 1005

Gorosabel, J., Pérez-Ramírez, D., Sollerman, J., et al. 2005, A&A, 444, 711
Gruendl, R. A., Chu, Y.-H., Dunne, B. C., & Points, S. D. 2000, AJ, 120, 2670
Hjorth, J., Sollerman, P., Møller, P., et al. 2003, Nature, 423, 847
Holland, S. T., Weidinger, M., Fynbo, J. P. U., et al. 2003, AJ, 125, 2291
Humphreys, R. M., & Davidson, K. 1994, PASP, 106, 1025
Jakobsson, P., Björnsson, G., Fynbo, J. P. U., et al. 2005, MNRAS, 362, 245
Jensen, B. L., Fynbo, J. P. U., Gorosabel, J., et al. 2001, A&A, 370, 909
Kann, D. A., Klose, S., & Zeh, A. 2006, ApJ, 641, 993
Kann, D. A., Masetti, N., & Klose, S. 2007, AJ, 133, 1187
Kann, D. A., Klose, S., Zhang, B., et al. 2010, ApJ, submitted [arXiv:0712.2186v2]
Kawabata, T., Matsumoto, K., Ayani, K., et al. 2004, IBVS, 5576
Kennicutt, R. C., Tamblyn, P., & Congdon, C. E. 1994, ApJ, 435, 22
Klose, S., Greiner, J., Rau, A., et al. 2004, AJ, 128, 1942
Langer, N., Hamann, W.-R., Lennon, M., et al. 1994, A&A, 290, 819
Langer, N., García-Segura, G., & Mac Low, M.-M. 1999, ApJ, 520, L49
Lazzati, D., Rossi, E., Covino, S., Ghisellini, G., & Malesani, D. 2002, A&A, 396, L5
Lazzati, D., Perna, R., Flasher, J., Dwarkadas, V. V., & Fiore, F. 2006, MNRAS, 372, 1791
Maeder, A. 1983, A&A, 120, 113
Maeder, A., & Meynet, G. 2000, A&A, 361, 159
Más-Hesse, J. M., Kunth, D., Tenorio-Tagle, G., et al., Star Formation through Time, ed. E. Pérez, R. González-Delgado, & G. Tenorio-Tagle, PASP Conf. Ser., 297, 177
Matheson, T., Garnavich, P. M., Foltz, C., et al. 2003, ApJ, 582, L5
Metzger, M. R., Djorgovski, S. G., Kulkarni, S. R., et al. 1997, Nature, 387, 878
Mirabal, N., Halpern, J. P., Chornock, R., et al. 2003, ApJ, 595, 935
Møller, P., Jakobsen P., & Perryman, M. A. C. 1994, A&A, 287, 719
Møller, P., Warren, S. J., Fall, S. M., Fynbo, J. P. U., & Jakobsen, P. 2002a, ApJ, 574, 51
Møller, P., Fynbo, J. P. U., Hjorth, J., et al. 2002b, A&A, 396, L21
Osterbrock, D. E. 1989, Astrophysics of Gaseous Nebulae and Active Galactic Nuclei (University Science Books, Mill Valley)
Pandey, S., Sahu, D. K., Resmi, L., et al. 2003, Bull. Astro. Soc. India, 31, 19
Pooley, G. 2002a, GCN Circ., 1575, http://gcn.gsfc.nasa.gov/gcn3/1575.gcn3
Pooley, G. 2002b, GCN Circ., 1588, http://gcn.gsfc.nasa.gov/gcn3/1588.gcn3
Prochaska, J. X., Chen, H.-W., & Bloom, J. S. 2006, ApJ, 648, 95
Prochaska, J. X., Dessagues-Zavadsky, M., & Ramirez-Ruiz, E. 2008, ApJ, 685, 344
Salamanca, I., Rol, E., Wijers, R. A. M. J., et al. 2002, GCN Circ., 1611, http://gcn.gsfc.nasa.gov/gcn3/1611.gcn3
Salvaterra, R., Della Valle, M., Campana, S., et al. 2009, Nature, 461, 1258
Sako, M., & Harrison, F. A. 2002a, GCN Circ., 1624, http://gcn.gsfc.nasa.gov/gcn3/1624.gcn3
Sako, M., & Harrison, F. A. 2002b, GCN Circ., 1716, http://gcn.gsfc.nasa.gov/gcn3/1716.gcn3
Sargent, W. L. W., Boksenberg, A., & Steidel, C. C. 1988, ApJS, 68, 539
Savaglio, S., Fiore, F., Israel, G., et al. 2002, GCN Circ., 1633, http://gcn.gsfc.nasa.gov/gcn3/1533.gcn3
Schaefer, B. E., Gerardy, C. L., Höflich, P., et al. 2003, ApJ, 588, 387
Shin, M.-S., Berger, E., Penprase, B. E., et al. 2006, unpublished [arXiv:astro-ph/0608327]
Shirasaki, Y., Graziani, C., Matsuoka, M., et al. 2002, GCN Circ., 1565, http://gcn.gsfc.nasa.gov/gcn3/1565.gcn3
Smith, L. J., Pettini, M., Dyson, J. E., & Hartquist, T. W. 1984, MNRAS, 211, 679
Srianand, R., Petitjean, P., Ledoux, C., & Hazard, C. 2002, MNRAS, 336, 753
Stanek, K., Matheson, T., Garnavich, P. M., et al. 2003, ApJ, 591, L17
Starling, R. L. C., Wijers, R. A. M. J., Hughes, M. A., et al. 2005, MNRAS, 360, 305
Tanvir, N. R., Barnard, V. E., Blain, A. W., et al. 2004, MNRAS, 352, 1073
Tanvir, N. R., Fox, D. B., Levan, A. J., et al. 2009, Nature, 461, 1254
Tejos, N., Lopez, S., Prochaska, J. X., Chen, H.-W., & Dessauges-Zavadsky, M. 2007, ApJ, 671, 622
Tejos, N., Lopez, S., Prochaska, J. X., et al. 2009, ApJ, 706, 1309
Tenorio-Tagle, G., Silich, S. A., Kunth, D., Terlevich, E., & Terlevich, R. 1999, MNRAS, 309, 332
Thöne, C. C., Greiner, J., Savaglio, S., & Jehin, E. 2007, ApJ, 671, 628
Uemura, M., Kato, T., Ishioka, R., & Yamaoka. H. 2003, PASJ, 55, L31
Vergani, S., D., Petitjean, P., Ledoux, C., et al. 2009, A&A, 503, 771
Vreeswijk, P. M., Ledoux, C., Smette, A., et al. 2007, A&A, 468, 83
Wang, L., Baade, D., Höflich, P., & Wheeler, J. C. 2003, unpublished [arXiv:astro-ph/0301266]
Woosley, S. E., & Bloom, J. S. 2006, ARA&A, 44, 507
Woosley, S. E. 1993, ApJ, 405, 273